

# Carrier Relaxation and Lattice Heating Dynamics in Silicon Revealed by Femtosecond Electron Diffraction<sup>†</sup>

Maher Harb, Ralph Ernstorfer, Thibault Dartigalongue, Christoph T. Hebeisen, Robert E. Jordan, and R. J. Dwayne Miller\*

*Institute for Optical Sciences and Departments of Physics and Chemistry, University of Toronto, 80 St. George Street, Toronto, Ontario M5S 3H6, Canada*

*Received: July 21, 2006; In Final Form: September 14, 2006*

We report on the use of femtosecond electron diffraction to resolve the dynamics of electron–phonon relaxation in silicon. Nanofabricated free-standing membranes of polycrystalline silicon were excited below the damage threshold with 387 nm light at a fluence of 5.6 mJ/cm<sup>2</sup> absorbed (corresponding to a carrier density of  $2.2 \times 10^{21}$  cm<sup>-3</sup>). The diffraction pattern was captured over a range of delay times with a time resolution of 350 fs. All of the detected Bragg peaks exhibited intensity loss with a time constant of less than 2 ps. Beyond the initial decay, there was no further change in the diffracted intensity up to 700 ps. We find that the loss of intensity in the diffracted orders is accounted for by the Debye–Waller effect on a time scale indicative of a thermally driven process as opposed to an electronically driven one. Furthermore, the relaxation time constant is consistent with the excitation regime where the phonon emission rate is reduced due to carrier screening.

## Introduction

The dynamics of photoexcited electrons in semiconductors and metals have been extensively studied within the last two decades.<sup>1,2</sup> On the ultrafast time scale, there are two dominant processes: Electron–electron scattering causes an energy redistribution of the carriers, whereas electron–phonon scattering governs the relaxation of the carriers, i.e., the energy transfer from the hot electrons to the lattice. The dynamics of the energy transfer also determines the dynamics of subsequent responses of the lattice like thermally driven phase transitions or electronically driven nonthermal melting.<sup>3–6</sup> The latter is believed to occur when more than 10% of the valence electrons are promoted to the conduction band.<sup>7</sup> The population of antibonding states causes a weakening of the covalent bonding in semiconductors that results in the disorder of the lattice before it reaches the equilibrium melting temperature. This phenomenon is characterized by a time scale that is much faster than that of a thermally driven process. Therefore it is important to understand the dynamics of electron–phonon relaxation in a purely thermal process. Ultrafast photoelectron dynamics are mainly studied by either time-resolved photoelectron spectroscopy,<sup>8–11</sup> which allows for a direct mapping of the transient energy distribution of the electrons, or time-resolved spectroscopy, which probes an optical response that is sensitive to carrier distribution, i.e., the electronic response of the solid after photoexcitation (e.g., reflectivity,<sup>4</sup> second harmonic generation<sup>12</sup>). Alternatively, it is possible to study carrier relaxation into acoustic phonon modes on picosecond time scales by using transient grating excitation to selectively couple light diffraction to surface acoustic waves driven by carrier relaxation.<sup>13–15</sup> All of these methods are either indirect probes of the lattice phonons or intrinsically limited in time resolution. The ideal probe with respect to following the carrier relaxation into specific lattice

degrees of freedom would be one capable of directly probing the distribution of phonons excited during carrier relaxation to lower *k*-states. In this regard, time-resolved X-ray diffraction<sup>16–18</sup> and electron diffraction<sup>19–22</sup> experiments are nearly ideal tools for studying the lattice deformations that accompany carrier relaxation. This information is particularly relevant to the control and manipulation of carrier relaxation to prevent energy loss in various solar cell implementations.<sup>23–24</sup> This interest was originally peaked by the work of Nozik and Ross that demonstrated that it is theoretically possible to increase solar energy conversion for a threshold absorber such as a semiconductor from 33% maximum efficiency up to 66% for a single composite structure.<sup>25</sup> Given the growing importance of solar energy in energy resource management, the issue of controlling hot carrier relaxation through quantum confinement and various mechanisms of creating phonon bottlenecks to retard carrier cooling is a highly relevant and important problem. Up to now, time-resolved X-ray diffraction has offered higher time resolution than electron diffraction for the observation of the lattice aspects of the carrier relaxation dynamics. Experiments based on X-ray probe pulses have attained 100 fs time resolution, however, with only a few diffraction orders collected.<sup>16–17</sup> In contrast, femtosecond electron diffraction (FED) is capable of collecting a sufficient number of diffracted orders to reveal structural information particularly relevant to phase transitions but has up to now a somewhat lower time resolution than the best X-ray diffraction studies.

In an approach complementary to existing studies, we investigate the electron–phonon relaxation from the viewpoint of the lattice using a new generation of high-flux electron guns with pulse durations on the 300 fs time scale. The paper is organized as follows: First an innovative method used to fabricate free-standing membranes of polycrystalline silicon is introduced. These membranes allow probing the sample in a transmission configuration for the highest time resolution while minimizing contributions from surface effects that may occur in a reflection geometry. Next, the Experimental Section gives

<sup>†</sup> Part of the special issue “Arthur J. Nozik Festschrift”.

\* Author to whom correspondence should be addressed. E-mail: dmiller@lphys.chem.utoronto.ca.

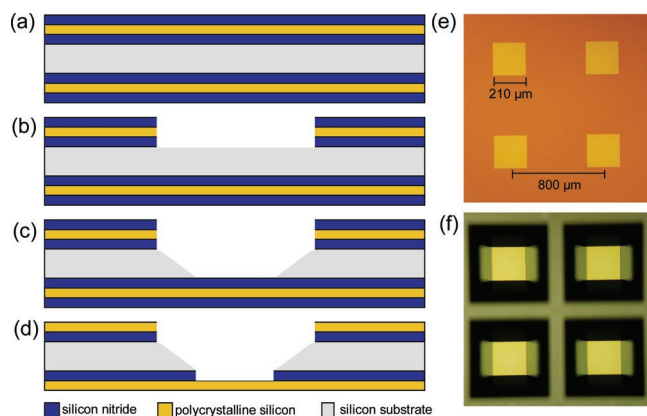


**Figure 1.** Schematic diagram of the sample after the main fabrication processes (a–d, not to scale) and pictures of the fabricated membranes (e–f). (a) Thin films are deposited on the silicon substrate. (b) Grid features are created in the deposited layers using a combination of photolithography and reactive ion etching. (c) KOH etches through the substrate and stops at the silicon nitride layer. (d) Phosphoric acid removes the silicon nitride layer leaving a free-standing membrane of polycrystalline silicon. (e) A front view picture shows the membranes (yellow) in the same plane as the wafer surface (orange). (f) A back view picture shows the substrate columns (gray) and the membranes (yellow) at the bottom of the deep trenches (black).

a brief description of the 55 keV electron gun design responsible for generating the ultrashort electron pulses. The present work uses carrier excitation levels within fully reversible conditions to demonstrate the capabilities of the new gun design. Finally, results are presented in the form of decay traces of the detected diffraction orders. It is shown that the decay of the diffraction peak intensities is consistent with a Debye–Waller effect. The decay time constant is extracted and compared to recent optical studies.

### Sample Fabrication

One of the difficulties associated with transmission electron diffraction is sample preparation as the sample thickness must be on the order of the electron elastic mean free path given by

$$\Lambda_e = \frac{1}{N\sigma_e} \quad (1)$$

where  $N$  is the number density of atoms in the sample and  $\sigma_e$  is the elastic scattering cross-section.<sup>26</sup> For silicon, based on theoretical calculations of the scattering cross-section,<sup>27</sup>  $\Lambda_e \approx 40$  nm for an electron energy of 55 keV.

We created 50-nm-thick free-standing membranes of polycrystalline silicon using the following nanofabrication approach. In a series of low-pressure chemical vapor depositions, a polycrystalline silicon layer was sandwiched between two low-stress silicon nitride layers on an underlying silicon substrate (Figure 1a). A grid pattern was first created in a photoresist layer using standard photolithography and then transferred to the deposited layers via reactive ion etching (RIE) (Figure 1b). Potassium hydroxide (KOH) etch was used to create holes through the exposed features of the grid (Figure 1c). The narrowing of the holes by the etch process is a result of the high (100)/(111) selectivity, which effectively causes the etch to progress along the (111) plane, i.e., at an angle of  $54^\circ$  relative to the surface of the (100)-oriented wafer. The polycrystalline silicon layer is protected by silicon nitride as it is resistant to KOH. Finally, hot phosphoric acid etch was used to thin the silicon nitride leaving free-standing structures of polycrystalline silicon (Figure 1d). The timing of the etching needs to be

controlled to avoid residual silicon nitride and because overetching leads to the destruction of most of the membranes due to their fragility. In these experiments, there was no evidence of residual silicon nitride in the diffraction pattern. For a detailed review of the mechanisms, etch rates, and selectivities of the used etching techniques, refer to ref 28.

Figures 1e and 1f are pictures of the fabricated membranes. The sample consists of an array of membranes, each  $210 \times 210 \mu\text{m}^2$  in dimension, supported by the remaining grid-like substrate. The sample was designed with a sufficient number of membranes to allow irreversible excitation, i.e., experiments where damage occurs from a single laser shot. These studies will be reported elsewhere.<sup>29</sup> Electron transmission through the membranes was measured by placing a Faraday cup at the position of the undiffracted beam. At the experimental electron energy of 55 keV the membranes exhibited  $\sim 50\%$  undiffracted transmission.

### Experimental Section

The main component of the FED setup is an electron gun capable of delivering femtosecond electron pulses. This is achieved by back-illuminating a 40-nm-thick silver photocathode with the third harmonic (centered around 258 nm) of a Ti:sapphire regenerative amplifier with a frequency-doubled femtosecond Er:fiber laser as the input seed. The third harmonic was generated by sequential type-I second harmonic generation and type-II sum frequency generation using two  $\beta$ -barium borate crystals. A fused silica prism compressor separated the harmonics and compensated the dispersion in the beam path. The duration of the fundamental pulse was characterized via autocorrelation measurements and found to be 180 fs full width at half-maximum (fwhm). To a good approximation, the initial temporal profile of the photoemitted electron pulse is determined by the duration of the tripled laser pulse. However, as the electron pulse propagates space-charge effects (repulsive forces) cause it to broaden.<sup>30</sup> We employed a compact electron gun design to limit space-charge effects. Electrons were accelerated to 55 keV kinetic energy over a distance of 6 mm, i.e., with an electric field close to the vacuum breakdown limit of  $\sim 10$  MV/m. The electron pulse was then collimated using a magnetic lens and scattered off the sample. The diffraction patterns were captured on a microchannel plate/phosphor screen detector with a charge coupled device (CCD) camera. The experiment was carried out under a high vacuum environment with a base pressure of  $10^{-7}$  mbar. The described design represents a significant advance in compact electron gun designs for problems requiring the highest time resolution. The high number of electrons per pulse is an important feature of the gun design. This feature is most relevant to irreversible samples, which are anticipated to be the general case for time-resolved electron diffraction studies of systems undergoing significant structural changes. In the case of a reversible sample, as in this current study, this design allows the acquisition of high signal-to-noise data in short periods of time.

Aside from the gun geometry, the electron pulse duration is mainly determined by the density of the photoemitted electron bunch. Higher electron densities lead to stronger space-charge fields that in turn cause a greater spreading of the pulse. Space-charge effects are difficult to predict due to the fact that (except for an ideal ellipsoidal bunch with a uniform charge distribution) the fields have a nonlinear effect on the velocity–position correlation of the phase space of the electron bunch.<sup>31</sup> We rely on  $N$ -body simulations using the Barnes–Hut<sup>30,32</sup> algorithm to model the pulse propagation dynamics. Under our experimental

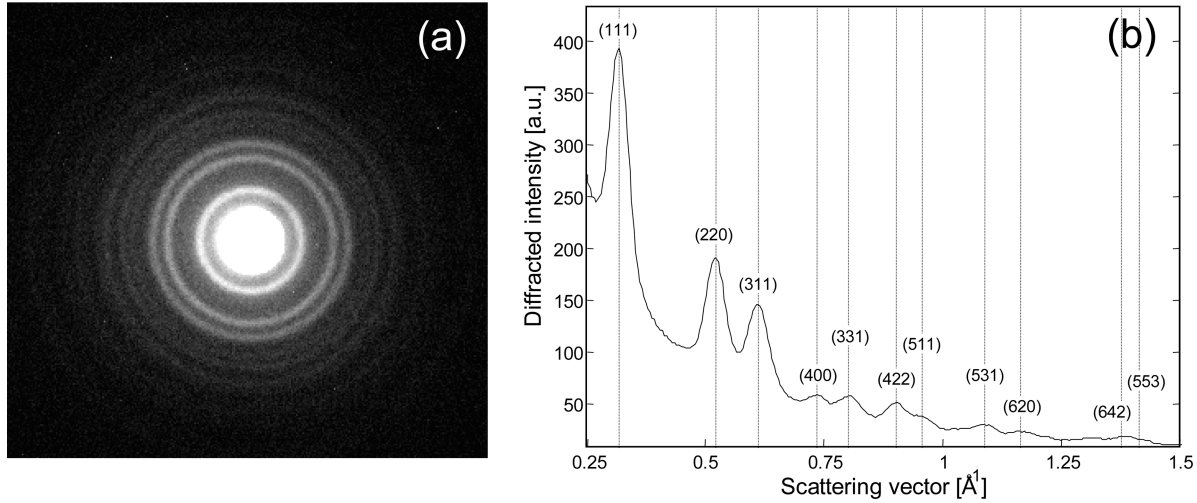


**Figure 2.** (a) Diffraction pattern of a silicon membrane taken under the same conditions as for the time-resolved experiment (center spot scaled separately to emphasize the diffraction rings). (b) Corresponding radial intensity average. (Dashed lines are theoretical peak positions of a diamond lattice structure with a lattice constant of 5.43 Å.)

conditions, i.e., a third harmonic spot size of 200  $\mu\text{m}$  (fwhm) at the photocathode and a total of 10 000 emitted electrons, results indicate that 3200 electrons pass through a 150  $\mu\text{m}$  diameter pinhole and reach the sample with a pulse duration of 300 fs (fwhm). The electron spot size was measured to be 150  $\mu\text{m}$  (fwhm) at the sample position. Recently, we established a technique that makes use of the ponderomotive force to directly measure the duration of an electron bunch as it crosses a highly intense laser pulse.<sup>33</sup> The technique has been applied to a slightly different gun geometry. The outcome of the ponderomotive experiment confirmed the validity of  $N$ -body simulations.

The sample was optically excited with the second harmonic of the laser system centered at 387 nm and focused to a spot size of 350  $\mu\text{m}$  (fwhm). The observed damage threshold was determined to be 6.5 mJ/cm<sup>2</sup> absorbed, although the maximum equilibrium sample temperature at this fluence falls short of the melting temperature (calculation based on eq 2 below). Under these excitation conditions, we interpret the damage to occur due to thermally induced mechanical stresses on the membrane. The experiment was performed at a fluence of 5.6 mJ/cm<sup>2</sup> chosen below the damage threshold to induce a thermally driven process.

## Results and Discussion

The excitation intensity of 5.6 mJ/cm<sup>2</sup> used in these experiments corresponds to a photoexcited carrier density  $N$  of  $2.2 \times 10^{21} \text{ cm}^{-3}$ , assuming single-photon absorption across the direct band gap of silicon. As noted earlier, nonthermal effects are expected at excitation densities greater than 10% of the valence electron density<sup>7</sup> of  $2 \times 10^{23} \text{ cm}^{-3}$ , which is clearly not the case here. A further advantage of operating below the damage threshold is the ability to probe the sample at a high repetition rate compared to that of the single shot limit (500 Hz in this experiment). Through the use of the thermo-physical properties of bulk silicon,<sup>34</sup> the rise in sample temperature  $\Delta T$  can be estimated with the following expression

$$\Delta T = F_{\text{abs}} \left( 1 - \frac{E_g}{h\nu} \right) \frac{1}{L} \frac{1}{\rho S} \quad (2)$$

where  $E_g$  is the silicon energy band gap,  $h$  is Planck's constant,  $\nu$  is the optical frequency of the pump pulse,  $L$  is the sample thickness,  $\rho$  is the density of silicon,  $S$  is its specific heat, and

$F_{\text{abs}}$  is the absorbed fluence given by

$$F_{\text{abs}} = aE(1 - R)(1 - \exp(-\alpha L))(1 + R \exp(-\alpha L)) \quad (3)$$

where  $E$  is the laser pulse energy,  $R$  is the reflectivity of the membranes, and  $\alpha$  is the absorption coefficient of silicon ( $2 \times 10^5 \text{ cm}^{-1}$  from ref 35). The reflectivity was measured to be  $\sim 50\%$ , which is in good agreement with the expected value of 53% (ref 35). Equation 3 accounts for the back-reflection of the pump light reaching the second surface of the membrane. The resulting transmission of the sample was verified through measurements and found to be  $\sim 10\%$ . The factor  $a$  in eq 3 accounts for the pump-probe overlap profile given by

$$a = \int_0^\infty 2\pi r \, dr \left( \frac{\exp(-r^2/w_{\text{pump}}^2)}{\pi w_{\text{pump}}^2} \right) \left( \frac{\exp(-r^2/w_{\text{probe}}^2)}{\pi w_{\text{probe}}^2} \right) = \frac{1}{\pi(w_{\text{pump}}^2 + w_{\text{probe}}^2)} \quad (4)$$

where  $w_{\text{pump}}$  and  $w_{\text{probe}}$  are the respective spot widths of the pump and probe beams (defined as the fwhm/(2  $\sqrt{\ln 2}$ )).

Equation 2 accounts for the excess energy of electrons and holes above the conduction band minimum (CBM) and below the valence band maximum (VBM), respectively. However, at these excitation levels, Auger recombination also occurs on the picosecond time scale. This three-body relaxation pathway provides an additional source term for lattice heating that constitutes the remaining 34% of the absorbed fluence. Auger recombination is usually described by  $\partial N/\partial t = -CN^3$ , where  $C$  is the Auger recombination coefficient.<sup>36</sup> A numerical solution of the above equation indicates that 66% of the energy deposited through Auger recombination is transferred to the carriers within 2 ps. Taking this effect into account, the result is a rise in temperature of 510 K to give a lattice temperature of approximately 800 K, well below the melting point of Si at 1683 K.

Diffraction images were captured before and during excitation with a varying delay between pump and probe pulses ranging from  $-5$  to  $+10$  ps with 333 fs steps. Each diffraction image was the result of an accumulation of  $\sim 10^7$  electrons. The diffraction image of a silicon membrane and its corresponding radially averaged intensity are shown in Figure 2. The nine main diffraction orders, up to the detector limit at  $1.5 \text{ Å}^{-1}$ , were



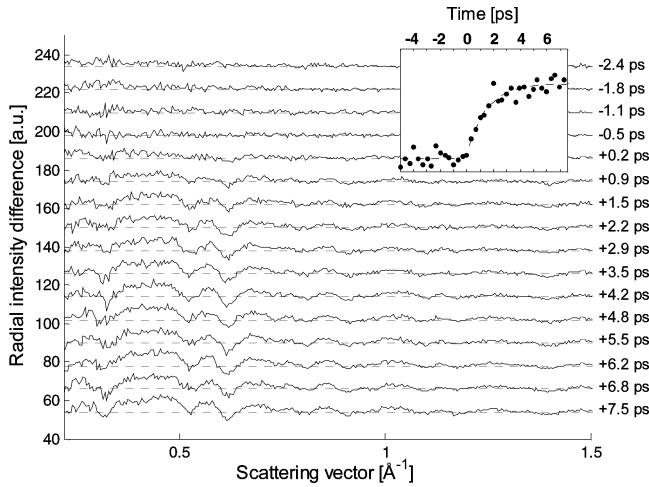


**Figure 3.** Radially averaged intensity difference of “during” excitation and “before” excitation diffraction images at selected time points. Dashed lines are the  $x$ -axes for each time point. An artificial offset is introduced between curves for clarity. The inset shows the change in the total inelastic scattering intensity between the (111) and the (220) peaks (dots) and a monoexponential fit with a time constant of 1.5 ps (dashed line).

captured with a sufficient signal-to-noise ratio to resolve the lattice dynamics. Figure 3 shows the intensity difference at selected time positions computed by subtracting the radial intensities of the diffraction images captured before excitation from the images captured during excitation. The decrease of the Bragg peak intensities, emerging as a negative signal at positive time delays in Figure 3, marks the onset of lattice heating. This effect is accompanied by an increase in inelastic scattering<sup>37</sup> evident by the rise of diffraction intensity between the Bragg peaks. The temporal evolution of the change of diffraction intensity between the (111) and (220) peaks is shown as an inset in Figure 3. This change is well described with a monoexponential rise with a time constant of  $1.5 \pm 0.4$  ps. This monoexponential fit to the inelastic scattering intensity was used to determine time zero, i.e., the temporal overlap of pump and probe pulses. Time zero was also independently determined by exciting a transmission electron microscopy grid at the sample position above the plasma generation threshold as described previously.<sup>22</sup> The relative changes of the amplitudes of various Bragg peaks are plotted in Figure 4. The amplitudes were computed by splitting the radially averaged intensity into three sections and fitting each to an  $n$ -Gaussian function with an exponential background. Such partitioning of the diffraction data was necessary since the background cannot be represented by a single-exponential function over the whole  $s$  range due to the inelastic scattering dynamics. As expected, the relative change of the peak amplitudes due to lattice heating increases with higher diffraction order due to the Debye–Waller effect.<sup>38</sup> The decay curves of the Bragg peaks at positive delay were fitted with the monoexponential function

$$f_{(hkl)}(t) = (1 - A_{(hkl)}) + A_{(hkl)} \exp[-t/\tau_{(hkl)}] \quad (5)$$

where  $(hkl)$  are the Miller indices and  $A_{(hkl)}$  and  $\tau_{(hkl)}$  are fit parameters representing the relative amplitude loss at long times ( $A_{(hkl)} = f_{(hkl)}(0) - \lim_{t \rightarrow \infty} f_{(hkl)}(t)$ ) and the decay time constant, respectively. The result of this fit is summarized in Table 1. The experiment was extended to +700 ps with no observed change in the diffracted intensity beyond the initial decay.

We first examine the decay data from the aspect of the amplitude loss. In a thermally driven process, this is accounted

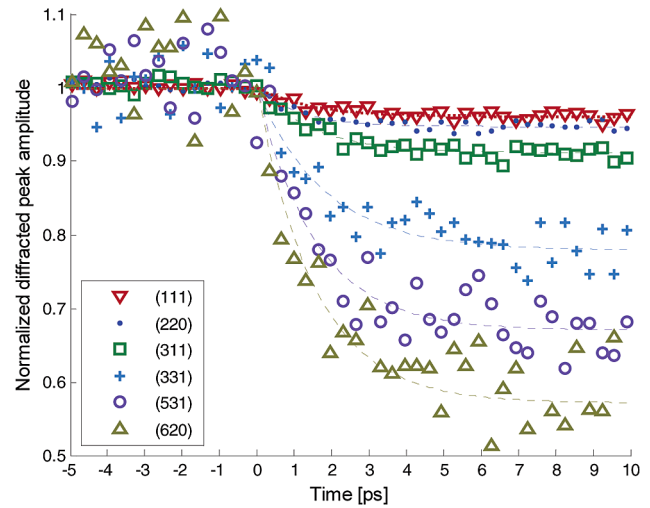


**Figure 4.** Decay traces for selected diffraction peaks. The amplitudes were normalized by the average amplitude at negative time points. The dashed curves are exponential fits of the traces.

for by the Debye–Waller effect. The diffracted intensity at a temperature  $T$  is<sup>38</sup>

$$I_{(hkl)}(T) = I_{(hkl)}(0) \exp[-s^2 B(T)] = I_{(hkl)}(T_R) \exp[-s^2 (B(T) - B(T_R))] \quad (6)$$

where  $s$  is the scattering vector,  $T_R$  is room temperature, and  $B(T)$  is the Debye–Waller factor. We based our analysis on values of  $B(T)$  obtained from the parametrization by Gao derived from experimental phonon density of states data.<sup>39</sup> The relative intensity loss becomes

$$\frac{I_{(hkl)}(T_R) - I_{(hkl)}(T)}{I_{(hkl)}(T_R)} = 1 - \exp[-s^2 (B(T) - B(T_R))] \quad (7)$$

At each time point, we performed a global fit of eq 7 to all  $A_{(hkl)}$  values with the temperature  $T$  as the only fit parameter. The resulting temperature evolution curve is shown in Figure 5. For long delays, a temperature change of  $494 \pm 28$  K accounts for the observed lattice dynamics. This temperature is in good agreement with the 510 K estimate based on bulk properties. The calculated amplitude loss at this heating level is listed in Table 1. By fitting the temperature evolution curve to a monoexponential function we extract a heating time constant  $\tau = 2.0 \pm 0.5$  ps. This number agrees with decay time constants of the individual diffraction orders ( $1.4 \pm 0.6$  ps) and with the rise time of the inelastic scattering intensity ( $1.5 \pm 0.4$  ps).

The initial energy redistribution of the carriers or electron thermalization due to electron–electron scattering is expected to occur within less than 150 fs.<sup>9</sup> The carriers then relax to the CBM (or VBM) via emission of longitudinal optical phonons to give the above effective lattice temperature. Reported time scales of this process range from a few hundreds of femtoseconds to a few picoseconds. The electron–phonon relaxation rate is highly dependent on the density of the excited carriers.<sup>40</sup> At high carrier densities the relaxation rate is reduced due to screening of the phonon modulation of the charge distribution within the lattice. According to Yoffa,<sup>40</sup> the reduced relaxation rate can be expressed as

$$\tau = \tau_0 \left[ 1 + \left( \frac{N}{N_c} \right)^2 \right] \quad (8)$$

**TABLE 1: Diffraction Order Decay Data<sup>a</sup>**

peak	(111)	(220)	(311)	(400)	(331)	(422)	(531)	(620)
time constant (ps)	2.0	1.2	1.6	2.0	1.4	1.6	1.2	1.9
amplitude loss	0.044	0.057	0.094	0.24	0.22	0.24	0.34	0.45
predicted amplitude loss for $\Delta T = 494$ K	0.040	0.10	0.14	0.19	0.23	0.27	0.37	0.42

<sup>a</sup> The time constant and amplitude loss obtained from fitting the decay traces to an exponential function. The last row is the calculated amplitude loss for a heating of 494 K assuming a strictly thermal process.

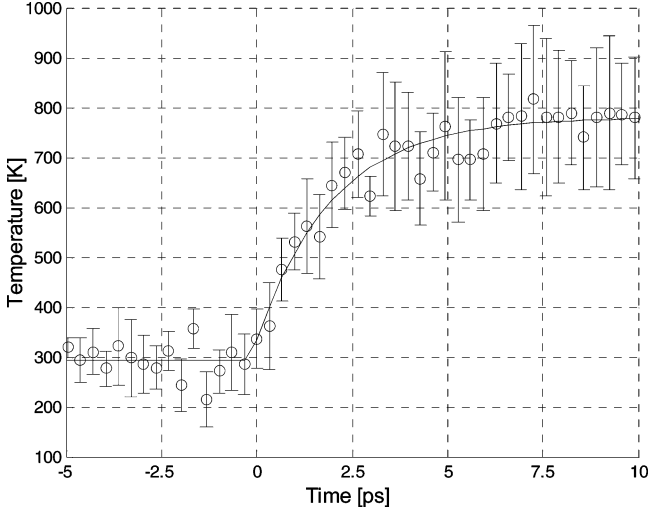


**Figure 5.** Temperature evolution of the sample constructed from decay data by fitting the amplitude loss at every time point to a model based on the Debye–Waller effect. Error bars represent the standard deviation of the individual peak temperatures. From a monoexponential fit (solid line) we extract a heating time constant of 2 ps.

where  $N_c$  is the critical carrier density at which screening becomes important and  $\tau_0$  is the screening-independent relaxation time. In a time-resolved photoemission study by Jeong et al., 200 fs relaxation time was reported for excitation energies above the bulk CBM and at very low carrier densities.<sup>10</sup> Under similar excitation conditions, Sjodin et al. observed a relaxation time of 240 fs using transient reflective grating methods,<sup>13</sup> and Sabbah et al. extracted a relaxation time of 260 fs through pump–probe reflectivity measurements.<sup>41</sup> Assuming  $\tau_0 = 230$  fs from the above findings, we deduce  $N_c = 8 \times 10^{20} \text{ cm}^{-3}$ , close to the theoretical value predicted by Yoffa<sup>40</sup> ( $1 \times 10^{21} \text{ cm}^{-3}$ ).

As Auger recombination and carrier screening effects are occurring on the same time scale, it is not possible to clearly distinguish the two mechanisms. The amount of energy dissipated through Auger recombination at the excitation wavelength and carrier densities used is on the order of 34%. Therefore, this source term will not dominate the lattice heating. There are also other competing processes that tend to retard the carrier relaxation. It has now been well established that at very high carrier injection levels a bottleneck in the phonon relaxation rate occurs.<sup>42</sup> The characteristic signature of the hot phonon bottleneck is the occurrence of relaxation features on the 10–100 ps time scale<sup>43</sup> due to thermal diffusion of both hot carriers and phonons into the bulk of the semiconductor. For the samples used in our studies, the excitation profile and ballistic electron transport ensure a uniform carrier distribution whereby these slower relaxation features are absent. There would be a fast carrier relaxation phase without the ensuing diffusion processes and further relaxation. In addition, the much larger carrier effective masses involved in the thermalization relaxation dynamics of Si in these experiments, as opposed to near-band-edge excitation of GaAs and related III–V semiconductors

where this effect has been observed, makes this mechanism less likely. The density of states suitable for conserving energy and momentum in the relaxation process is much higher in Si such that phonon bottlenecks are less of a contributing factor to the retardation of the carrier thermalization. On the above considerations and the good agreement with expected carrier thermalization rates with screening effects included, we attribute the observed carrier relaxation dynamics to carrier screening effects.

A carrier injection level dependence will help to further confirm this mechanism. With the compact electron gun design, the spatial resolution is compromised for time resolution. Further improvements in femtosecond electron gun designs with improved spatial coherence are in progress that will lead to an increase in the electron source brightness by several orders of magnitude and will enable a complete mapping of carrier relaxation into the different phonon branches for an atomic level description of electron–phonon coupling.

## Conclusion

We demonstrated the use of FED to resolve the dynamics of electron–phonon relaxation. The time scale of relaxation is consistent with findings from optical pump–probe studies and carrier screening of electron–phonon coupling at high injection levels. The changes in the diffraction amplitudes as the lattice is heated agree with the Debye–Waller factors, which unambiguously identify the decay process as a strictly thermal one. The carrier injection levels used are below the threshold for previously predicted nonthermal-driven phase transitions and provide a good baseline for purely thermal effects. At higher excitations, we expect a clear transition into a regime where electronic factors dominate in semiconductors, leading to nonthermal melting. This regime is quite distinctive from the thermally driven phase transitions observed in metals<sup>19,22</sup> and will underscore the fundamental differences in the (directionality of) bonding between metals and semiconductors. Finally, we note that the nanofabrication technique introduced in these experiments represents an important advance in providing the sample film for time-resolved diffraction experiments. This approach helps in properly defining time zero across an extended sample area required for irreversible experiments without elaborate sample mapping procedures. In addition, it provides nanometer-sized free-standing films suitable for electron diffraction in the transmission mode for the highest time resolution. This sample configuration also provides a solution for time-resolved X-ray diffraction experiments involving strongly absorbed pump light. This procedure could be applied to other semiconductors such as GaAs using molecular beam epitaxy methods with differential etching to provide single crystal domains. The extension to single crystals would offer greater detection sensitivity and the ability to pump and probe-specific modes for higher spatial resolution.

**Acknowledgment.** We thank the Cornell NanoScale Science and Technology Facility and the Emerging Communications Technology Institute at the University of Toronto for providing

us access to their facilities to fabricate the silicon membranes. This work was supported by the Natural Sciences and Engineering Research Council of Canada, and the Canadian Foundation for Innovation. R.E. thanks the Alexander-von-Humboldt Foundation for financial support.

## References and Notes

- (1) Shah, J. *Solid-State Electron.* **1989**, 32, 1051.
- (2) Othonos, A. *J. Appl. Phys.* **1998**, 83, 1789.
- (3) Callan, J. P.; Kim, A. M. T.; Luang, L.; Mazur, E. *Chem. Phys.* **2000**, 251, 167.
- (4) Shank, C. V.; Yen, R.; Hirlimann, C. *Phys. Rev. Lett.* **1983**, 50, 454.
- (5) Sokolowski-Tinten, K.; Bialkowski, J.; von der Linde, D. *Phys. Rev. B* **1995**, 51, 14186.
- (6) Tom, H. W. K.; Aumiller, G. D.; Brito-Cruz, C. H. *Phys. Rev. Lett.* **1988**, 60, 1438.
- (7) Graves, J. S.; Allen, R. E. *Phys. Rev. B* **1998**, 58, 627.
- (8) Schmittenmaier, C.; Miller, C. C.; Herman, J.; Cao, J.; Gao, Y. L.; Mantell, D.; Miller, R. J. D. *Chem. Phys.* **1996**, 205, 91.
- (9) Goldman, J. R.; Prybyla, J. A. *Phys. Rev. Lett.* **1994**, 72, 1364.
- (10) Jeong, S.; Zacharias, H.; Bokor, J. *Phys. Rev. B* **1996**, 54, 17300.
- (11) Rowe, M. W.; Liu, H.; Williams, G. P., Jr.; Williams, R. T. *Phys. Rev. B* **1993**, 47, 2048.
- (12) Shank, C. V.; Yen, R.; Hirlimann, C. *Phys. Rev. Lett.* **1983**, 51, 900.
- (13) Sjodin, T.; Petek, H.; Dai, H. *Phys. Rev. Lett.* **1998**, 81, 5664.
- (14) Kasinski, J. J.; Gomez-Jahn, L.; Gracewski, S. M.; Faran, K. J.; Miller, R. J. D. *J. Chem. Phys.* **1989**, 90, 1253.
- (15) Morishita, T.; Hibara, A.; Sawada, T.; Tsuyumoto, I.; Harata, A. *Anal. Sci.* **2000**, 16, 403.
- (16) Rousse, A.; Rischel, C.; Fourmaux, S.; Uschmann, I.; Sebban, S.; Grillon, G.; Balcou, Ph.; Förster, E.; Geindre, J. P.; Audebert, P.; Gauthier J. C.; Hulin, D. *Nature (London)* **2001**, 410, 65.
- (17) Lindenberg, A. M.; Larsson, J.; Sokolowski-Tinten, K.; Gaffney, K. J.; Blome, C.; Synnergren, O.; Sheppard, J.; Coleman, C.; MacPhee, A. G.; Weinstein, D.; Lowney, D. P.; Allison, T. K.; Matthews, T.; Falcone, R. W.; Cavalleri, A. L.; Fritz, D. M.; Lee, S. H.; Bucksbaum, P. H.; Reis, D. A.; Rudati, J.; Fuoss, P. H.; Kao, C. C.; Siddons, D. P.; Pahl, R.; Als-Nielsen, J.; Duesterer, S.; Ischebeck, R.; Schlarb, H.; Schulte-Schrepping, H.; Tschentscher, Th.; Schneider, J.; von der Linde, D.; Hignette, O.; Sette, F.; Chapman, H. N.; Lee, R. W.; Hansen, T. N.; Techert, S.; Wark, J. S.; Bergh, M.; Huidt, G.; van der Spoel, D.; Timneanu, N.; Hajdu, J.; Akre, R. A.; Bong, E.; Krejcik, P.; Arthur, J.; Brennan, S.; Luening, K.; Hastings J. B. *Science* **2005**, 308, 392.
- (18) Cavalleri, A.; Siders, C. W.; Rose-Petruck, C.; Jimenez, R.; Tóth, Cs.; Squier, J. A.; Barty, C. P. J.; Wilson, K. R. *Phys. Rev. B* **2001**, 63, 193306.
- (19) Siwick, B.; Dwyer, J. R.; Jordan, R. E.; Miller, R. J. D. *Science* **2003**, 302, 1382.
- (20) Ruan, C.-Y.; Lobastov, V. A.; Franco, V.; Chen, S.; Zewail, A. H. *Science* **2004**, 304, 974.
- (21) Cao, J.; Hao, Z.; Park, H.; Tao, C.; Kau, D.; Blaszczyk, L. *Appl. Phys. Lett.* **2003**, 83, 1044.
- (22) Dwyer, J. R.; Hebeisen, C. T.; Ernstorfer, R.; Harb, M.; Deyirmenjian, V. B.; Jordan, R. E.; Miller, R. J. D. *Philos. Trans. R. Soc. London, Ser. A* **2006**, 364, 741.
- (23) Nozik, A. J.; *Physica E* **2002**, 14, 115.
- (24) Miller, R. J. D. *Advances in Photoinduced Electron Transfer at Surfaces: A Decade in Perspective*; World Press: New Jersey, 1999.
- (25) Ross, R. T.; Nozik, A. J. *J. Appl. Phys.* **1982**, 53, 3813.
- (26) Reimer, L. *Transmission Electron Microscopy: Physics of Image Formation and Microanalysis*; Springer-Verlag: New York, 1984.
- (27) Riley, M. E.; MacCallum, C. J.; Biggs, F. *At. Data Nucl. Data Tables* **1975**, 15, 443.
- (28) Williams, K. R.; Muller, R. S. *J. Microelectromech. Syst.* **1996**, 5, 256.
- (29) Harb, M.; Ernstorfer, R.; Hebeisen, C. T.; Dartigalongue, T.; Jordan, R. E.; Miller, R. J. D., to be submitted for publication.
- (30) Siwick, B. J.; Dwyer, J. R.; Jordan, R. E.; Miller, R. J. D. *J. Appl. Phys.* **2002**, 92, 1643.
- (31) Luiten, O. J.; van der Geer, S. B.; de Loos, M. J.; Kiewiet, F. B.; van der Wiel, M. J. *Phys. Rev. Lett.* **2004**, 93, 094802.
- (32) Barnes, J.; Hut, P. *Nature (London)* **1986**, 324, 446.
- (33) Hebeisen, C. T.; Ernstorfer, R.; Harb, M.; Dartigalongue, T.; Jordan, R. E.; Miller, R. J. D. *Opt. Lett.*, in press.
- (34) Desai, P. D. *J. Phys. Chem. Ref. Data* **1986**, 15, 967.
- (35) *Handbook of Chemistry and Physics*, 86th ed.; CRC Press: Boca Raton, FL, 2005.
- (36) Svantesson, K. G.; Nilsson, N. G. *J. Phys. C: Solid State Phys.* **1979**, 12, 5111.
- (37) Dudarev, S. L.; Peng, L.-M.; Whelan, M. J. *Phys. Rev. B* **1993**, 48, 13408.
- (38) Kittel, C. *Introduction to Solid State Physics*; Wiley: New York, 1986.
- (39) Gao, H. X.; Peng, L.-M. *Acta Crystallogr., Sect. A: Found. Crystallogr.* **1999**, 55, 926.
- (40) Yoffa, E. J. *Phys. Rev. B* **1981**, 23, 1909.
- (41) Sabbah, A. J.; Riffe, D. M. *Phys. Rev. B* **2002**, 66, 165217.
- (42) van Driel, H. M. *Phys. Rev. B* **1979**, 19, 5928.
- (43) Nozik, A. J. *Annu. Rev. Phys. Chem.* **2001**, 52, 193.